

Electronic Transport in Graphitic Nanoribbon Films

Ashkan Behnam,^{†,§} Jason L. Johnson,^{†,§} Yanbin An,[†] Amlan Biswas,[‡] and Ant Ural^{†,*}

[†]Department of Electrical and Computer Engineering and [‡]Department of Physics, University of Florida, Gainesville, Florida 32611, United States. [§]These authors contributed equally to this work.

Similar to carbon nanotube and nanowire networks, films and composites made up of graphene sheets have also recently demonstrated potential as conductive, transparent, and flexible materials.^{1–9} These films can be produced by relatively low-cost and simple fabrication methods such as chemical processing of graphite or graphene oxide pallets^{1–5} and chemical vapor deposition.^{6,7} So far, the focus of most of the research related to graphitic films and composites has been on the development and simplification of the fabrication process,^{1,4–7} as opposed to fundamental electrical characterization of the material. Electrical characterization of these films and composites is important in order to shed light on the basic transport mechanisms and their inherent structural properties, before they can be optimized for various device applications. Structural properties, such as the density, area, and aspect ratio of the nanoscale elements, making up these films and composites affect both the transparency and conductivity of the material, as shown by various theoretical studies on nanocomposites.^{10–12} For instance, a recent computational study advocates increasing the aspect ratio of the sheets to obtain a material with relatively low graphene sheet density (and hence high transmittance) and high conductance.¹⁰

In this paper, we (1) successfully fabricate and analyze the structure of films composed of long and narrow multilayer graphene nanoribbons and (2) study the low-temperature transport and its dependence on electric and magnetic fields in these materials. We use a simple chemical procedure for film fabrication and then pattern the films into four-point-probe structures using photolithography and plasma etching. Our fabrication and patterning approach can be optimized and applied to a variety of graphene-based materials. Using various

ABSTRACT We fabricate, pattern, and analyze thin films composed of multilayer graphene nanoribbons. These films are conductive at room temperature but depict noticeable insulating behavior at low temperatures (<20 K) due to their disordered structure. We study the transport in this strong localization regime by analyzing the dependence of resistivity on temperature and electric and magnetic fields in the framework of the variable range hopping theory. Resistivity dependence on the magnetic field confirms the insulating behavior of the films and can be fitted effectively by forward interference scattering and wave function shrinkage models at low and high magnetic field regimes, respectively. We extract large localization lengths in the range of ~45–90 nm from both the magnetic and electric field dependence of resistivity and relate these values to the high conductance in the nanoribbons and/or good contact between them. By revealing the fundamental structural and transport properties of graphitic nanoribbon films, our results help devise methods to further improve these films for electronic and photonic device applications.

KEYWORDS: graphitic · nanoribbon · film · resistivity · variable range hopping · localization · magnetoresistance

characterization techniques, we confirm that individual or bundles of narrow and long nanoribbons composed of multiple graphene layers are the elements that form the film. We then analyze the film resistivity and its variation as a function of temperature and applied electric and magnetic fields at low temperatures in the framework of the variable range hopping theory. Results presented here not only provide information on the physics of electronic transport in these graphitic nanoribbon films but also help evaluate their suitability and improve their properties for potential device applications.

RESULTS AND DISCUSSION

Figures 1a and 1c show transmission electron microscopy (TEM) and atomic force microscopy (AFM) images, respectively, of a thin graphitic nanoribbon film (GNF). A careful analysis of many similar TEM and AFM images suggests that most individual nanoribbons in the GNF have thicknesses between 3 and 15 nm (average about 7.5 nm), widths between 3 and 13 nm (average about

*Address correspondence to abehnam@ufl.edu, antural@ufl.edu.

Received for review April 22, 2010 and accepted January 31, 2011.

Published online February 22, 2011
10.1021/nn100855n

© 2011 American Chemical Society

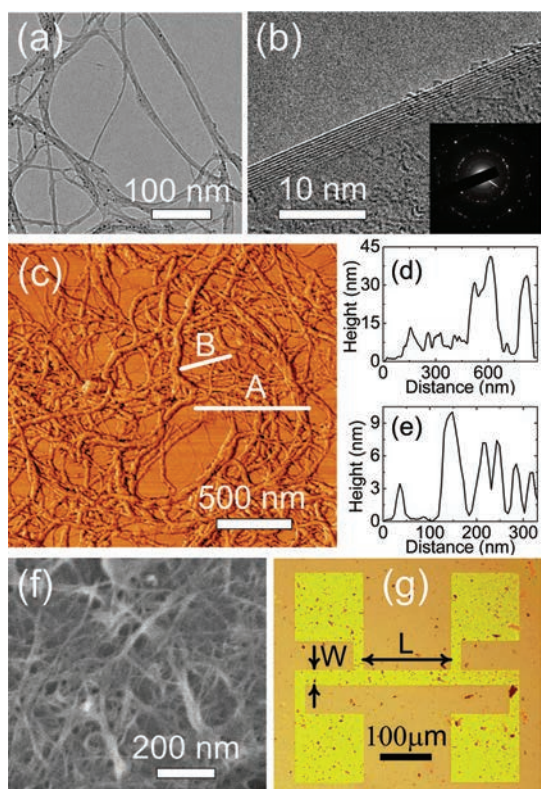


Figure 1. (a) Transmission electron microscopy (TEM) image of graphitic nanoribbons. (b) High-resolution TEM image of the folded edge of an individual graphitic ribbon, where the nine graphene layers forming the ribbon are visible. The inset shows the selected area electron diffraction (SAED) pattern for the same nanoribbon. (c) Atomic force microscopy (AFM) phase image of a thin graphitic nanoribbon film (GNF). (d,e) Height profile of the AFM image along the lines A and B shown in (c), respectively. (f) Scanning electron microscope (SEM) image of a ~ 60 nm thick GNF. (g) Optical microscope image of a four-point-probe device structure patterned from a 60 nm GNF on a SiO_2 substrate using photolithography and reactive ion etching. The width W and length L of the device are labeled in the figure.

6.6 nm), and lengths between 500 nm and a few micrometers. Figure 1b is a TEM image of the folded edge of a ribbon illustrating the ~ 9 graphene layers that form the ribbon. Selected area electron diffraction (SAED) pattern in the inset of Figure 1b shows several concentric rings representative of multilayer graphene.^{13,14} While there are many individual nanoribbons in the GNF, often the ribbons also form bundles with thicknesses as high as ~ 60 nm and widths as wide as ~ 50 nm. The AFM height profiles in Figures 1d and 1e are obtained from Figure 1c along the lines labeled A and B, respectively, and contrast the thickness of single ribbons (Figure 1e) and bundles (right side of Figure 1d). The scanning electron microscope (SEM) image in Figure 1f shows the morphology of a ~ 60 nm thick GNF. The uniformity of a GNF improves, and its resistance decreases significantly as its thickness increases. More quantitative structural analysis, including statistical information regarding the width

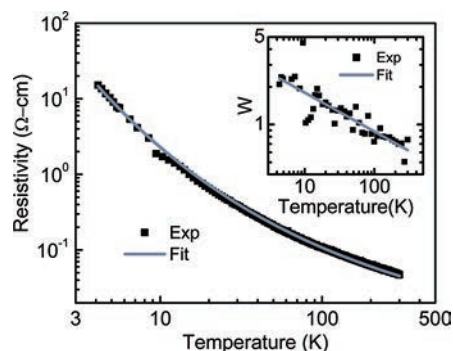


Figure 2. Log–log plot of resistivity (ρ) versus T for a GNF four-point-probe device structure with $L = 1500 \mu\text{m}$, $W = 50 \mu\text{m}$, and $t = 60$ nm. The black squares are experimental data points, while the gray curve is the fit to the experimental results based on the variable range hopping (VRH) model. The inset depicts the log–log plot of reduced activation energy (W) versus T with the gray curve being a power-law fit to the data.

and thickness distribution of the nanoribbons, as well as Raman spectroscopy, X-ray photoelectron spectroscopy (XPS), and transmittance measurement results are provided in the Supporting Information. Raman and XPS results and the electrical measurements discussed below confirm the graphitic nature of the ribbons despite the presence of a small amount of oxygen bonding groups and defects in their structure.

Figure 1g depicts the optical microscope image of a patterned GNF four-point-probe device structure with $30 \mu\text{m}$ width (W) and $200 \mu\text{m}$ length (L), marked with arrows in the figure. The room temperature resistance was measured for several four-point-probe device structures with lengths ranging from 200 to $1500 \mu\text{m}$, widths ranging from 10 to $100 \mu\text{m}$, and thicknesses of 60 and 120 nm. For all of these devices, room temperature resistivities (ρ) are found to be within the range of $0.045\text{--}0.075 \Omega \cdot \text{cm}$ and do not scale with device dimensions. This is because the device dimensions are significantly larger than the size of nanoribbons making up the film, and hence the devices are well above the percolation threshold.^{15,16}

Figure 2 shows a log–log plot of ρ versus temperature (T) for a GNF device with length $L = 1500 \mu\text{m}$, width $W = 50 \mu\text{m}$, and thickness $t = 60$ nm. It is evident from the figure that ρ increases over 2 orders of magnitude as T decreases from 300 to 4.2 K, thus showing a strong insulating behavior that is due to the localization of carriers at low temperatures. To confirm the insulating behavior of the film at low temperatures, reduced activation energy (W), defined as

$$W(T) = -\frac{d \ln(\rho(T))}{d \ln T} \quad (1)$$

is calculated and plotted in the inset of Figure 2 as a function of T . The increase in W as the temperature decreases suggests a nonzero value for W at $T = 0$ K and a transport mechanism that can be explained by Mott variable range hopping (VRH).¹⁷ For VRH transport,

ρ can be written as

$$\rho(T) = C \exp[(T_0/T)^p] \quad (2)$$

where C is a constant, T_0 is the characteristic temperature that is proportional to the energy separation between the available states, and $p = 1/(d + 1)$ for Mott VRH,¹⁷ where $d = 1, 2,$ or 3 is the dimensionality of the hopping conduction. The value of p can be extracted from the slope of the W versus T plot in the inset of Figure 2. The rest of the parameters can then be determined by fitting eq 2 directly to the ρ versus T plot, as shown in the main panel of Figure 2. The values thus extracted for p , C , and T_0 are ~ 0.31 , $0.005 \Omega \cdot \text{cm}$, and 4200 K , respectively. The value extracted for p (*i.e.*, 0.31) is closer to 0.33 expected for 2D Mott VRH transport than to 0.25 expected for 3D Mott VRH transport. This behavior can be related to either the structure of the film which is not completely 3D (the transport could be partially 2D in larger ribbons) or alternatively to a transition from Mott VRH to coulomb gap (CG) VRH, for which the extracted exponent p is expected to have a value close to 0.5 .¹⁸ The value extracted for T_0 (*i.e.*, 4200 K) can be used to determine another temperature parameter T_1 below which VRH transport is valid. This temperature corresponds to the limit at which the optimum hopping distance is equal to the localization length and therefore can be extracted from $1 = ((1-p)/2)(T_0/T_1)^p$ based on the VRH transport theory.¹⁸ For our device, the extracted value is 135.8 K , which shows that VRH can indeed explain the electronic transport at low temperatures.

In order to further investigate the transport in the VRH regime, we have studied the electric and magnetic field dependences of resistivity at low temperatures. The top right inset of Figure 3 shows I – V characteristics of our device at four different temperatures in the range of 4.2 – 20 K . It is evident that the I – V curve transitions from linear to nonlinear behavior as the temperature decreases. To better present the effect of electric field (E) at low temperatures on the transport in the film, differential device resistance as a function of E is shown in the main panel of Figure 3 for the same temperatures as in the inset. As can be seen, the change in the differential resistance within the measured E -field range decreases and the threshold electric field required for the onset of nonlinearity (E_{th}) increases as the temperature increases. While at low temperatures and very low fields, the hopping transport is induced by phonons, at intermediate fields, the electric field can contribute to the energy necessary for the carriers to hop. In this regime, resistance has an exponential dependence on the electric field.¹⁹ Still at stronger fields, electric field-based hopping becomes dominant and the resistance becomes temperature-independent. In this regime, the differential resistivity obeys $\rho(E) \propto \exp[(E_0/E)^m]$, where E_0 and m are constants. This equation is similar to the temperature

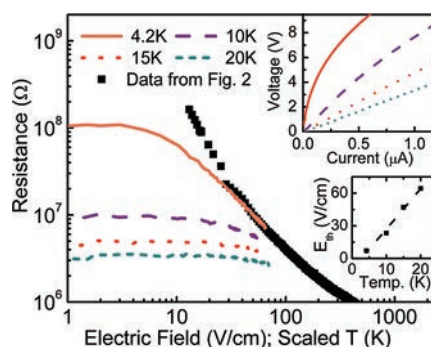


Figure 3. Log–log plot of the differential resistance versus electric field E for the device in Figure 2 at four different temperatures, as labeled. The black squares are the experimental resistance versus temperature data points (from the main panel of Figure 2) scaled to fit the differential resistance versus E results. The top right inset shows the I – V characteristics for the same device at the same temperatures as in the main panel. The bottom right inset is a plot of the extracted threshold electric field E_{th} as a function of temperature.

dependence of resistivity in the VRH regime at low fields as given by eq 2.^{20,21} Also shown in the main panel of Figure 3 is the dependence of resistance on temperature for our device (*i.e.*, the data already shown in the main panel of Figure 2) that is scaled to fit the other four curves in the high electric-field region.²¹ This fitting is allowed because the dependence of the resistance on the E -field at high electric fields follows the same form as the dependence of the resistance on temperature at low electric fields, although experimental data at higher fields would be needed for a quantitative analysis based on this fit.^{20,21} The similarity between the electric field (4.2 K) and temperature dependence of the resistance in the high field region is clear from this fitting.

One of the important parameters in analyzing disordered systems in the VRH regime is the localization length a . At the onset of nonlinearity, the hopping energy provided by the electric field and temperature become comparable and the relationship between E_{th} and T becomes $qE_{\text{th}}a/k_{\text{B}}T = 0.2$,^{20,21} where q is the electron charge and k_{B} is the Boltzmann constant. We have used different $R(E_{\text{th}})/R(0)$ ratios (between 0.80 and 0.95) to define the onset of nonlinearity and extract E_{th} . An example is shown in the bottom right inset in Figure 3, where we have extracted E_{th} as the E -field at which $R(E_{\text{th}})/R(0) = 0.8$. The linear relationship between E_{th} and T is clear in this inset. The value of the localization length a can be extracted from the slope of the E_{th} versus T plot. The extracted a values were within the range of 45 – 90 nm , depending on the $R(E_{\text{th}})/R(0)$ ratio used (0.80 – 0.95) in the definition of E_{th} . The large value of the extracted a might be related to the long length of the nanoribbons in the film that are conductive even at low temperatures.

Last, we turn to the study of the effect of magnetic field on the transport. The main panel of Figure 4a

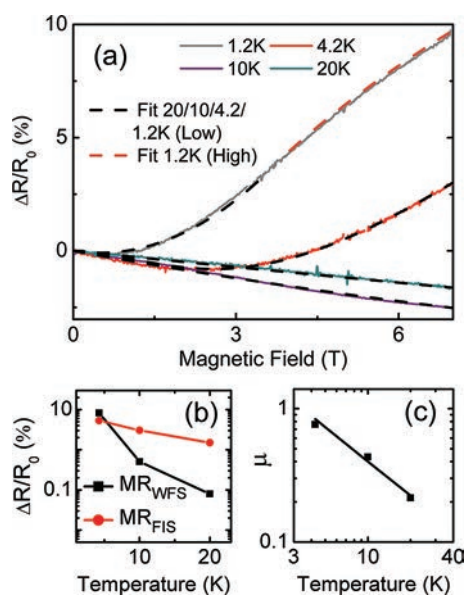


Figure 4. (a) Experimental magnetoresistance (MR) data for our device at four different temperatures as labeled. The black dashed curves are fits to the experimental data using eq 3 in the text. The orange dashed curve is a fit to the high field range of the 1.2 K MR data as explained in detail in the text. (b) Contribution of forward interference scattering (MR_{FIS}) and wave function shrinkage (MR_{WFS}) to the total magnetoresistance as a function of temperature at a magnetic field of 7 T. (c) Log–log plot of the temperature dependence of the coefficient μ defined in the text. From the slope of the fit shown by the solid line, $\beta = 0.86$ is extracted.

shows magnetoresistance (MR) data for our device at four different temperatures up to ~ 7 T. As can be seen, while at higher temperatures, MR is negative and decreases with magnetic field (B), and at very low temperatures, it reaches a negative minimum and then starts to increase and finally obtains positive values at high B . The positive sign of the second derivative of the MR, that is $d^2MR/dB^2|_{B=0}$ as $T \rightarrow 0$ is a signature of strong localization.²²

On the basis of the VRH theory, the negative contribution to the MR data in Figure 4a is most likely due to forward interference scattering (FIS),^{23–25} while the positive contribution to the MR is probably due to wave function shrinkage (WFS).^{23,25} In the FIS model, direct and indirect hopping mechanisms between localized states are considered, and the phase factor that is introduced by the field flux through the area between the hopping routes is averaged to show that the field reduces the resistance.^{23–25} On the other hand, in the WFS model, the magnetic field decreases the overlap probability between two localized states and thereby the resistance increases. In the Mott VRH regime, due to the strong localization of the states and weak interaction between the carriers, the WFS model is more appropriate for explaining the MR data compared to the spin effect models.^{26,27} The contributions from FIS and WFS models can be added up and then

fitted to the experimental MR data. The complete equation can be written as

$$\begin{aligned} MR &= \frac{\Delta R}{R_0} = MR_{\text{FIS}} + MR_{\text{WFS}} \\ &= -\alpha T^{-\beta} B + \gamma(T) B^2 \end{aligned} \quad (3)$$

where MR_{FIS} and MR_{WFS} are the negative FIS and positive WFS contributions to magnetoresistance, respectively; α is a constant, γ is a temperature-dependent coefficient, and β is the temperature dependence exponent of the forward interference scattering term. In the VRH region, β should be close to 1 for a 2D system and close to 7/8 for a 3D one.²⁴

As can be seen from the fitted curves shown in Figure 4a, the above simple model in eq 3 can explain the MR trends at low and high fields well except for the relative saturation of the 1.2 K curve at fields higher than 4 T, which will be discussed below. Figure 4b shows the positive and negative fitted contributions to the MR as a function of T . As expected,^{23,26} FIS portion (negative contribution) gradually becomes weaker as T goes up but is still significant at 20 K. On the other hand, WFS portion (positive contribution) is more sensitive to T and vanishes quickly as T goes up to 10 K. Figure 4c shows the log–log plot of μ versus T , where μ is defined as the magnitude of the coefficient in front of B in the FIS term in eq 3 (i.e., $\mu = \alpha T^{-\beta}$). From the slope of Figure 4c, β is determined to be 0.859, which is close to the theoretical prediction of $\beta \cong 7/8$ for a 3D system.²⁴ In Figures 4b and 4c, the 1.2 K data points are omitted due to the nonideality of the fit to the 1.2 K MR curve, especially at high magnetic fields. FIS and WFS models explain, respectively, that at high fields the negative contribution to the MR approaches a constant value²⁵ instead of depending linearly on B (due to the induced symmetry by the magnetic field) and the positive contribution scales with $B^{1/3}$ instead of B^2 (ref 26) (due to the stronger magnetic field-induced transverse localization compared to the Coulomb potential-induced localization). Magnetic field thresholds for the onset of these two transitions are very close to each other, and both depend strongly on T . In the case of our films, these thresholds are already outside the range of the measured fields for MR data above 1.2 K, and therefore, the model presented in eq 3 is valid for fitting those three curves. However, the 1.2 K MR data begin to deviate from eq 3 above ~ 4 T. Using an expression for MR suggested for a Mott VRH system for high magnetic fields,^{26,28} namely, $MR = -t + (e/6\hbar)^{1/3} (T_0/T)^{1/3} a^{2/3} B^{1/3}$, we have fitted the high field range of the MR at 1.2 K, as shown in the main panel of Figure 4a. In this equation, t is a constant at a fixed temperature and a is the localization length defined before.^{26,28} The fit results in a localization length of about $a = 68$ nm, in agreement with the range obtained from the electric field dependence of

resistance. On the basis of the above results, it can be seen that WFS and FIS models explain all of the MR data successfully and the VRH theory not only successfully explains the T and E dependence of resistance but also provides very good fitting results for the MR data.

CONCLUSIONS

In summary, we have fabricated and patterned thin films of graphitic nanoribbons and studied the low-temperature electronic transport in these films. These films are composed of long and narrow multilayer graphene nanoribbons, as evidenced by AFM, TEM, SEM, and Raman characterization. The nanoribbon films depict insulating behavior at very low temperatures, which is expected due to the disordered nature of the films and can be explained by Mott VRH. Furthermore, the film resistivity depends on both electric and magnetic fields at temperatures lower

than 20 K. Resistivity dependence on the electric field is significant at fields higher than 10 V/cm and follows the VRH theory. From that dependence, the localization length is extracted to be between 45 and 90 nm. This large value of the localization length is likely due to the high conductance in the nanoribbons and/or good contact between them. Resistivity dependence on the magnetic field confirms the insulating behavior of the films and can be fitted effectively by forward interference scattering and wave function shrinkage models. These models can also explain the saturation of the MR data at 1.2 K. The localization length of ~ 68 nm extracted from the MR data is in agreement with the value extracted from the electric field dependence. The results presented here not only reveal the fundamental transport mechanisms in graphitic nanoribbon films but also help evaluate and improve them for electronic and photonic device applications.

MATERIALS AND METHODS

Film Fabrication. The starting product was expanded flake graphite (product number 3775) provided by Asbury Carbons, Asbury, NJ. This product is made by intercalating flake graphite with sulfuric acid and heat treating the intercalated flakes to about 800 °C for exfoliation. The resultant material is then made into a powder. Graphitic nanoribbon films (GNFs) were produced by a vacuum-filtration process using this product as received. Briefly, 40 mg of expanded flake graphite and 2 g of sodium dodecylbenzene sulfonate (SDBS) surfactant were mixed in 200 mL of DI water. Strong sonication and centrifugation processes have been shown to generate graphene nanoribbons as opposed to larger sheets of graphene.²⁹ Therefore, the solution was agitated vigorously with a homogenizer for 1 h and then sonicated using a cup-horn sonicator (90 W) to obtain multilayer graphene nanoribbons. Next, the solution was centrifuged, and the supernatant was removed and vacuum filtered through an alumina filtration membrane with 100 nm pore size (Whatman, Inc.). A homogeneous GNF was deposited on the membrane by the filtration process with a thickness that could be controlled by the volume of the solution filtered and the density of the graphitic nanoribbons in the solution.^{30,31} After the film was dried, the supporting alumina filter was dissolved using a strong base solution and the nanoribbon film was transferred onto a silicon-based substrate. Finally, the sample was soaked in 1:3 solution of HCl and DI water to remove any remaining contaminants.

Device Fabrication. In order to prepare a GNF for electrical characterization, the film was patterned into four-point-probe device structures (to eliminate the contribution of contacts to the measured resistance) by photolithography and inductively coupled plasma reactive ion etching (ICP-RIE) using an O_2 chemistry.^{15,16} After GNF patterning, metal contact pads (20 nm Ti/150 nm Au) were deposited on the contact areas of the GNF using photolithography, e-beam evaporation, and subsequent lift-off. Gold wires (dipped in a conductive silver-based epoxy glue) were then used to connect to the four contacts. For low-temperature characterization, the sample was mounted in a helium cryostat equipped with a Janis variable-temperature insert and a superconducting magnet.

Acknowledgment. This work was funded in part by the Semiconductor Research Corporation. The authors would like to thank Asbury Carbons for kindly providing the expanded flake graphite, and Prof. K. Ziegler for access to his lab

equipment. J.L.J. acknowledges support from the U.S. National Science Foundation South East Alliance for Graduate Education and the Professoriate (SEAGEP) award. A.B. acknowledges the support of the U.S. National Science Foundation under Grant No. DMR 0804452.

Supporting Information Available: Quantitative structural analysis, including statistical information regarding the width and thickness distribution of the nanoribbons, as well as Raman spectroscopy, X-ray photoelectron spectroscopy (XPS), and transmittance measurement results. This material is available free of charge via the Internet at <http://pubs.acs.org>.

REFERENCES AND NOTES

1. Watcharotone, S.; Dikin, D. A.; Stankovich, S.; Piner, R.; Jung, I.; Dommett, G. H. B.; Evmenenko, G.; Wu, S. E.; Chen, S. F.; Liu, C. P.; *et al.* Graphene–Silica Composite Thin Films as Transparent Conductors. *Nano Lett.* **2007**, *7*, 1888–1892.
2. Xu, Y.; Bai, H.; Lu, G.; Li, C.; Gaoquan, S. Flexible Graphene Films via the Filtration of Water-Soluble Noncovalent Functionalized Graphene Sheets. *J. Am. Chem. Soc.* **2008**, *130*, 5856–5857.
3. Ramanathan, T.; Abdala, A. A.; Stankovich, S.; Dikin, D. A.; Herrera-Alonso, M.; Piner, R. D.; Adamson, D. H.; Schniepp, H. C.; Chen, X.; Ruoff, R. S.; *et al.* Functionalized Graphene Sheets for Polymer Nanocomposites. *Nat. Nanotechnol.* **2008**, *3*, 327–331.
4. Eda, G.; Chhowalla, M. Graphene-Based Composite Thin Films for Electronics. *Nano Lett.* **2009**, *9*, 814–818.
5. Stankovich, S.; Dikin, D. A.; Dommett, G. H. B.; Kohlhaas, K. M.; Zimney, E. J.; Stach, E. A.; Piner, R. D.; Nguyen, S. T.; Ruoff, R. S. Graphene-Based Composite Materials. *Nature* **2006**, *442*, 282–286.
6. Li, X.; Cai, W.; An, J.; Kim, S.; Nah, D. J.; Yang, D.; Piner, R.; Velamakanni, A.; Jung, I.; Tutuc, E.; *et al.* Large-Area Synthesis of High-Quality and Uniform Graphene Films on Copper Foils. *Science* **2009**, *324*, 1312–1314.
7. Kim, K.; Zhao, Y.; Jang, H.; Lee, S.; Kim, J.; Kim, K.; Ahn, J.; Kim, P.; Choi, J.; Hong, B. Large-Scale Pattern Growth of Graphene Films for Stretchable Transparent Electrodes. *Nature* **2009**, *457*, 706–710.
8. Hu, L.; Hecht, D. S.; Grüner, G. Infrared Transparent Carbon Nanotube Thin Films. *Appl. Phys. Lett.* **2009**, *94*, 081103.
9. Verdejo, R.; Barroso-Bujans, F.; Rodriguez-Perez, M. A.; Antonio de Saja, J.; Lopez-Manchado, M. A. Functionalized

- Graphene Sheet Filled Silicone Foam Nanocomposites. *J. Mater. Chem.* **2008**, *18*, 2221–2226.
- Hicks, J.; Behnam, A.; Ural, A. A Computational Study of Tunneling-Percolation Electrical Transport in Graphene-Based Nanocomposites. *Appl. Phys. Lett.* **2009**, *95*, 213103.
 - Dalmas, F.; Dendievel, R.; Chazeau, L.; Cavaille, J. Y.; Gauthier, C. Carbon Nanotube-Filled Polymer of Electrical Conductivity in Composites: Numerical Simulation Three-Dimensional Entangled Fibrous Networks. *Acta Mater.* **2006**, *54*, 2923–2931.
 - Foygel, M.; Morris, R. D.; Anez, D.; French, S.; Sobolev, V. L. Theoretical and Computational Studies of Carbon Nanotube Composites and Suspensions: Electrical and Thermal Conductivity. *Phys. Rev. B* **2005**, *71*, 104201.
 - Wang, X.; Zhi, L.; Müllen, K. Transparent, Conductive Graphene Electrodes for Dye-Sensitized Solar Cells. *Nano Lett.* **2008**, *8*, 323–327.
 - Reina, A.; Jia, X.; Ho, J.; Nezich, D.; Son, H.; Bulovic, V.; Dresselhaus, M. S.; Kong, J. Large Area, Few-Layer Graphene Films on Arbitrary Substrates by Chemical Vapor Deposition. *Nano Lett.* **2009**, *9*, 30–35.
 - Behnam, A.; Noriega, L.; Choi, Y.; Wu, Z.; Rinzler, A. G.; Ural, A. Resistivity Scaling in Single-Walled Carbon Nanotube Films Patterned to Submicron Dimensions. *Appl. Phys. Lett.* **2006**, *89*, 093107.
 - Behnam, A.; Choi, Y.; Noriega, L.; Wu, Z.; Kravchenko, I.; Rinzler, A. G.; Ural, A. Nanolithographic Patterning of Transparent, Conductive Single-Walled Carbon Nanotube Films by Inductively Coupled Plasma Reactive Ion Etching. *J. Vac. Sci. Technol., B* **2007**, *25*, 348–354.
 - Mott, N. F. *Metal-Insulator Transitions*, 2nd ed.; Taylor & Francis: London, 1990; pp 65–105.
 - Vavro, J.; Kikkawa, J. M.; Fischer, J. E. Metal-Insulator Transition in Doped Single-Wall Carbon Nanotubes. *Phys. Rev. B* **2005**, *71*, 155410.
 - Hill, P. M. Hopping Conduction in Amorphous Solids. *Philos. Mag.* **1971**, *24*, 1307–1325.
 - Fuhrer, M. S.; Holmes, W.; Richards, P. L.; Delaney, P.; Louie, S. G.; Zettl, A. Nonlinear Transport and Localization in Single-Walled Carbon Nanotubes. *Synth. Met.* **1999**, *103*, 2529–2532.
 - Apsley, N.; Hughes, H. P. Temperature-Dependence and Field-Dependence of Hopping Conduction in Disordered Systems. *Philos. Mag.* **1975**, *31*, 1327–1339.
 - Fung, A. W. P.; Dresselhaus, M. S.; Endo, M. Transport-Properties near the Metal-Insulator-Transition in Heat-Treated Activated Carbon-Fibers. *Phys. Rev. B* **1993**, *48*, 14953–14962.
 - Nguen, V. L.; Spivak, B. Z.; Shklovskii, B. I. Tunnel Hopping in Disordered Systems. *Sov. Phys. JETP* **1985**, *62*, 1021–1029.
 - Schirmacher, W. Quantum-Interference Magnetoconductivity in the Variable-Range-Hopping Regime. *Phys. Rev. B* **1990**, *41*, 2461–2468.
 - Sivan, U.; Entin-Wihlman, O.; Imry, Y. Orbital Magnetoconductance in the Variable-Range-Hopping Regime. *Phys. Rev. Lett.* **1988**, *60*, 1566–1569.
 - Shklovskii, B. I.; Efros, A. L. *Electronic Properties of Doped Semiconductors*, 2nd ed.; Springer-Verlog: Berlin, 1984; pp 202–222.
 - Kurobe, A.; Kamimura, H. Correlation-Effects on Variable Range Hopping Conduction and the Magnetoresistance. *J. Phys. Soc. Jpn.* **1982**, *51*, 1904–1913.
 - Rosenbaum, R.; Murphy, T.; Palm, E.; Hannahs, S.; Brandt, B. Magnetoresistance of Insulating Amorphous $\text{Ni}_x\text{Si}_{1-x}$ Films Exhibiting Mott Variable-Range Hopping Laws. *Phys. Rev. B* **2001**, *63*, 094426.
 - Li, X.; Wang, X.; Zhang, L.; Lee, S.; Dai, H. Chemically Derived, Ultrasoft Graphene Nanoribbon Semiconductors. *Science* **2008**, *319*, 1229–1232.
 - Li, D.; Müller, M. B.; Gilje, S.; Kaner, R. B.; Wallace, G. G. Processable Aqueous Dispersions of Graphene Nanosheets. *Nat. Nanotechnol.* **2008**, *3*, 101–105.
 - Wu, Z.; Chen, Z.; Du, X.; Logan, J.; Sippel, J.; Nikolou, M.; Kamaras, K.; Reynolds, J.; Tanner, D.; Hebard, A.; *et al.* Transparent, Conductive Carbon Nanotube Films. *Science* **2004**, *305*, 1273–1276.